



Radial and circular motion of photons and test particles in the Schwarzschild black hole with quintessence and string clouds

G. Mustafa^{1,a} , Ibrar Hussain^{2,b}

¹ Department of Mathematics, Shanghai University, Shanghai 200444, People's Republic of China

² School of Electrical Engineering and Computer Science, National University of Sciences and Technology, H-12, Islamabad, Pakistan

Received: 19 February 2021 / Accepted: 28 April 2021 / Published online: 13 May 2021

© The Author(s) 2021

Abstract The null and timelike geodesic motion in the vicinity of the Schwarzschild black hole in the presence of the string cloud parameter a and the quintessence field parameter q is studied. The ranges for both the parameters a and q are determined, which allow the existence of the black hole. In the radial motion of photon, the coordinate time t first decreases with the increasing values of both the parameters a and q and then in the close proximity of the horizon of the black hole, there is a turning point, after which the effect of the quintessence field is just opposite on the time t . For the massive particles, the proper time τ decreases with increasing values of the parameter a and increases with increase in the value of the parameter q . In the same case of the massive particles, the coordinate time t decreases with increase in the values of both the parameters a and q . Further, it is found that for test particles, the stable circular orbits exist in this spacetime for small values of both the parameters i.e., for $0 < a \ll 1$ and $0 < q \ll 1$. It is observed that the radii of the null circular orbits increase as the values of the parameters a and q increase. While in the case of the timelike geodesics, the radii of the circular orbits increase as the value of the parameter a increases, and they decrease as the value of the parameter q increases.

1 Introduction

The study of particle dynamics and photon orbits in black hole spacetimes is very important from the astrophysical point of view. This study enables us to comprehend the strong gravitational field around black holes. The recent observation of gravitational waves from the merger of binary black holes [1], has increased our interest in the investigation of the black hole dynamics. Particle motion in the vicinity of black holes

helps in understanding astrophysical phenomena such as perihelion shift, deflection of light, gravitational lensing, quasi-periodic oscillations of particles, and gravitational time dilation [2, 3]. The circular timelike and null geodesics explain the nature of the accretion disks around black holes where the particles are in circular motion. The investigation of the circular motion of photons around black holes may enhance our understanding of gravitational lensing, which is not only to distort the image of the background galaxy but can also amplify its light. The radial null and timelike geodesics describe the formation jets in black hole spacetimes where the particle moves radially. A vast literature exist on the timelike and null particle motion in black hole spacetimes [4–13]. Different authors have been considered charged and neutral particle motion in the vicinity of different static and rotating black holes with and without charge [14–19]. The effect of different fields, including magnetic field, quintessence field, perfect fluid, and string clouds, has been investigated on the motion of massive and massless particles around black holes [20–27]. Particle dynamics have also been discussed in the theories of gravity other than General Relativity, in order to obtain some constraints on the different parameters involved in the theories (see for example [28–35]).

The null and timelike geodesic motion for both the circular and radial cases in the Schwarzschild black hole has been analyzed [36, 37]. Israel has shown that in the Schwarzschild black hole, in the radial motion, particles appear to slow down as they fall towards the Schwarzschild black hole released from rest at infinity [38]. He has further observed that the circular orbits with radii less than three times the Schwarzschild radius are unstable. These geodesics have also been investigated in the AdS-Schwarzschild black hole spacetime, and the effect of the cosmological constant has been observed on the circular orbits of the particle [39]. Recently the effects of the string clouds, which are a collection of strings formed in the early stages in the development of our Universe due to symmetry breaking, have been investigated on the null and

^a e-mail: gmustafa3828@gmail.com (corresponding author)

^b e-mail: ibrar.hussain@seecs.nust.edu.pk

timelike geodesics around the Schwarzschild black hole [13]. There it has been observed that in the presence of the string cloud parameter, the radii of the circular orbits is bigger than the radii of the circular orbits in the Schwarzschild black hole in the absence of the string cloud parameter. Further, it is observed there, with the increase in the value of the string cloud parameter, the particle can more easily escape to infinity. In another recent work, the effect of the quintessence, which is an appealing candidate for the accelerated expansion of our Universe, has been studied on the motion of particles in the spacetime of the Schwarzschild black hole [12], where it is shown that the quintessence field pushes the circular orbits away from the central object, i.e., the radii of the circular orbits are larger than the radii of the circular orbits in the pure Schwarzschild case. Null particle dynamics in the Schwarzschild black hole with quintessence have been analyzed by Fernando for some particular values of the equation of state parameter [40].

In the present work, we are interested in investigating the null and the timelike geodesics in the Schwarzschild black hole in the presence of both the string clouds and quintessence to examine their combined effects on the motion of particles. The details are given in the subsequent sections. The work done here may be of interest in developing new tests of the theory of General Relativity to get corresponding constraints on the parameters involved here. In the next section, we study the radial motion for both massive and massless particles in the vicinity of the Schwarzschild black hole with quintessence and string clouds. In Sect. 3, we consider null and timelike circular geodesics in the spacetime geometry of the same black hole. The last section is devoted to the summary and discussion of our work.

2 Basic calculations of particle trajectories

The spherically symmetric and static spacetime in the background of quintessence and cloud of strings is given as [41, 42]:

$$\begin{aligned}
 ds^2 = & - \left(1 - a - \frac{2M}{r} - \frac{q}{r^{3\omega_q+1}} \right) dt^2 \\
 & + \left(1 - a - \frac{2M}{r} - \frac{q}{r^{3\omega_q+1}} \right)^{-1} dr^2 \\
 & + r^2(d\theta^2 + \sin^2\theta d\phi^2),
 \end{aligned} \tag{1}$$

where ω_q , M , a , and q are the equation of state parameter (EoS) for quintessence field, mass of the black hole, string cloud parameter, and quintessence parameter respectively. The EoS parameter for the quintessence field has the values, i.e., $-1 < \omega_q < -\frac{1}{3}$ [43]. The present study is restricted to the case when $\omega_q = -\frac{2}{3}$. In the absence of a and q , the above spacetime can be reduced to the Schwarzschild spacetime.

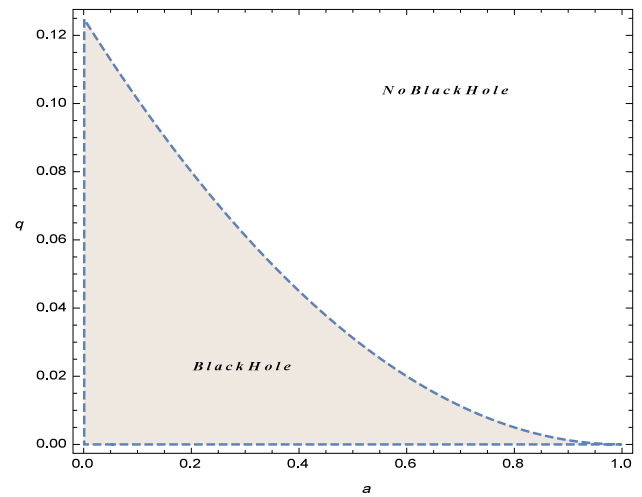


Fig. 1 Shows the trusted region, where we can discuss the geodesic motions of the black hole. The shaded region shows the constraint on the cloud of strings and quintessence parameters, i.e., $0 < a < 1$ and $0 < q < 0.125$

The horizon structure of the spacetime given by Eq. (1) for $\omega_q = -\frac{2}{3}$, is given as

$$\begin{aligned}
 r_q &= \frac{1 - a + \sqrt{a^2 - 2a - 8Mq + 1}}{2q}, \\
 r_e &= \frac{1 - a - \sqrt{a^2 - 2a - 8Mq + 1}}{2q}.
 \end{aligned} \tag{2}$$

For the quantity in the square root, in Eq. (2), to be positive we have $0 < q < \frac{a^2 - 2a + 1}{8M}$ and $0 < a < 1$. The root of the laps function, given by r_q , is the horizon due to the quintessence term, which corresponds to the cosmological horizon and the other root represented by r_e corresponds to the event horizon. The presence of the string clouds and quintessence field increase r_e . The r_e , in the required limits reduces to the horizon of the Schwarzschild spacetime i.e. when $a \rightarrow 0$ and $q \rightarrow 0$, $r_e = 2M$. From the intervals obtained here for q and a , we find the region for the existence of the black hole, presented in the Fig. 1.

The behavior of both the horizons, i.e., r_q and r_e can be seen from the Fig. 2 for the different possible values of the string cloud parameter a and the quintessence parameter q .

The Lagrangian for the metric given by Eq. (1) with $\omega_q = -\frac{2}{3}$ is

$$\begin{aligned}
 \mathcal{L} = & \frac{m}{2} g_{\mu\nu} \dot{y}^\mu \dot{y}^\nu = m \left(- \left(1 - a - \frac{2M}{r} - \frac{q}{r^{-1}} \right) \frac{\dot{t}^2}{2} \right. \\
 & \left. + \frac{\dot{r}^2}{2 \left(1 - a - \frac{2M}{r} - \frac{q}{r^{-1}} \right)} + \frac{r^2}{2} (\dot{\theta}^2 + \sin^2\theta \dot{\phi}^2) \right).
 \end{aligned} \tag{3}$$

For this Lagrangian we have the following two conserved quantities, the specific energy E and the specific angular

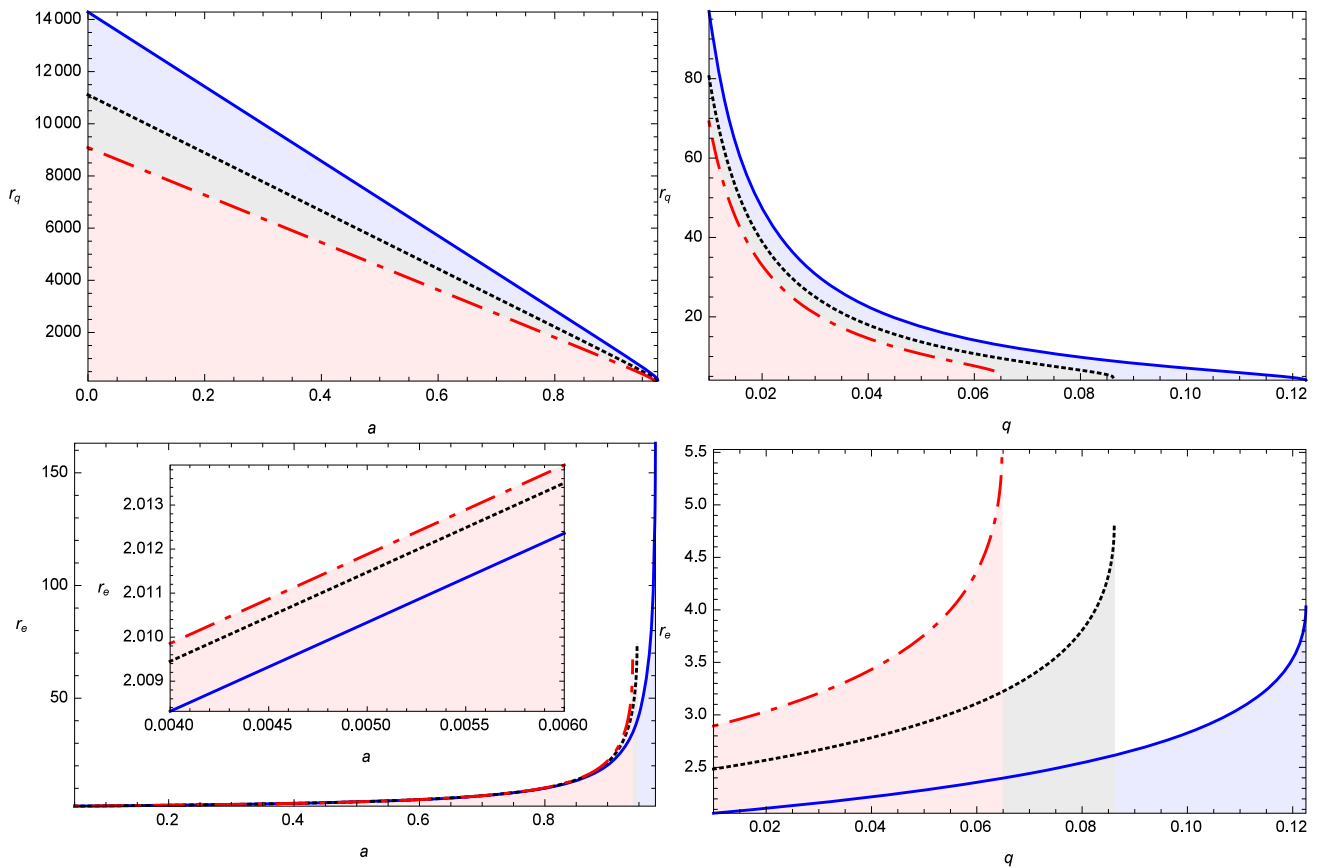


Fig. 2 Shows the graphic analysis of r_q in first row and r_e in second row for the different possible values of a and q . The left panel of the first row represents $q = 0.00007$ (blue), $q = 0.00009$ (black), and $q = 0.00011$ (red). The right panel of the first row represents

$a = 0.01$ (blue), $a = 0.17$ (black), and $a = 0.28$ (red). The left panel of the second row represents $q = 0.00007$ (blue), $q = 0.00009$ (black), and $q = 0.00011$ (red). The right panel of the second row represents $a = 0.01$ (blue), $a = 0.17$ (black), and $a = 0.28$ (red)

momentum L of the particle

$$i = -E \left(1 - a - \frac{2M}{r} - \frac{q}{r^{-1}} \right)^{-1}, \tag{4}$$

$$\dot{\phi} = \frac{L}{r^2 \sin^2 \theta}, \tag{5}$$

In the equatorial plane, i.e. we take $\theta = \frac{\pi}{2}$, Eq. (3) becomes

$$-\left(1 - a - \frac{2M}{r} - \frac{q}{r^{-1}} \right) i^2 + \frac{\dot{\phi}^2}{\left(1 - a - \frac{2M}{r} - \frac{q}{r^{-1}} \right)} + r^2 \dot{\phi}^2 = -\zeta, \tag{6}$$

where $\zeta = 0, 1$ is used to define the null and timelike geodesics respectively. Using the normalization condition $u^a u_a = -1$, the equation of motion is

$$\left(\frac{dr}{d\chi} \right)^2 + V_{eff}(r) = E^2, \tag{7}$$

where

$$V_{eff}(r) = \left(1 - a - \frac{2M}{r} - \frac{q}{r^{-1}} \right) \left(\zeta + \frac{L^2}{r^2} \right), \tag{8}$$

represents the effective potential.

3 Radial geodesic motion

In this section, we explore the radial geodesics of particles in the black hole spacetime given by Eq. (1). In this regard, $\dot{\phi} = 0$ and the angular momentum vanishes, i.e., $L = 0$. Now, Eq. (7) takes the following form

$$\left(\frac{dr}{d\chi} \right)^2 + \zeta \times \left(1 - a - \frac{2M}{r} - \frac{q}{r^{-1}} \right) = E^2. \tag{9}$$

3.1 Null radial geodesics

Here we discuss the null geodesics, i.e., the motion of massless particles by employing $\zeta = 0$ in Eq. (9), we obtain

$$\left(\frac{dr}{d\chi}\right)^2 = E^2. \tag{10}$$

From Eqs. (4) and (10), we get the following relation

$$\left(\frac{dr}{dt}\right) = \pm \left(1 - a - \frac{2M}{r} - \frac{q}{r^{-1}}\right). \tag{11}$$

Integrating Eq. (11) we arrive at the expression for the coordinate time t for the outgoing and ingoing photons as

$$t = \frac{\pm \log(r(a + qr - 1) + 2M) \mp \frac{2(a-1) \tan^{-1}\left(\frac{a+2qr-1}{\sqrt{8Mq-(a-1)^2}}\right)}{\sqrt{8Mq-(a-1)^2}}}{2q}. \tag{12}$$

From the Fig. 3 it can be seen that with an increase in the values of both the parameters a and q , the time t decreases and as the photon getting closer and closer to the horizon of the black hole, there appears a turning point, after which, the effect of the quintessence field is just opposite on the time t . It means that in the presence of the string clouds and quintessence, for an external observer the particle first moving faster towards the black hole and after passing the turning point then it slows down under the influence of the quintessence field. This observation shows that the particle takes shorter to reach the horizon as compared to the case of the pure Schwarzschild black hole [38].

3.2 Timelike geodesics

For the timelike geodesics, we choose $\zeta = 1$, and Eq. (9) becomes

$$\left(\frac{dr}{d\tau}\right) = \sqrt{E^2 - \left(1 - a - \frac{2M}{r} - \frac{q}{r^{-1}}\right)}. \tag{13}$$

The above Eq. (13) provides the following relation

$$\ddot{r} = -\frac{M}{r^2} - \frac{q}{2}. \tag{14}$$

The above Eq. (14), reduces to that of the equation of motion for the Schwarzschild case when $q = 0$ [36]. It should be noticed that the equation of motion (14), is independent of the parameter a as it was the case for the Schwarzschild black hole with string clouds [13]. Here we observe that the particle will accelerate more rapidly towards the central object in the presences of the quintessence field. Further we can see that there is no effect of the string clouds on the acceleration of the particle.

Now consider initially the particle is at rest i.e., $\dot{r} = 0$, and upon the gravitational attraction it accelerates towards the gravitating source from its initial location $r = r_0$. From Eq. (13) we have

$$E^2 = \left(1 - a - \frac{2M}{r_0} - \frac{q}{r_0^{-1}}\right) \tag{15}$$

and therefore

$$\left(\frac{dr}{d\tau}\right)^2 = 2M\left(\frac{1}{r} - \frac{1}{r_0}\right) + q\left(\frac{1}{r^{-1}} - \frac{1}{r_0^{-1}}\right). \tag{16}$$

In the limit $q \rightarrow 0$, the above Eq. (16), reduces to the corresponding equation in the Schwarzschild black case [38]. This shows that the gain in the kinetic energy of the particle in the radial motion, falling from rest at $r = r_0$, is equals to the sum of the loss in the gravitational potential energy of the particle and the contribution due to the quintessence dependent term. Further, we combine Eq. (13) with Eq. (4), and by sitting $E = 1$, we get the following expression

$$\frac{dt}{d\tau} = -\left(1 - a - \frac{2M}{r} - \frac{q}{r^{-1}}\right)^{-1} \tag{17}$$

and

$$\frac{dr}{d\tau} = \sqrt{\left(a + \frac{2M}{r} + \frac{q}{r^{-1}}\right)}. \tag{18}$$

On integrating this last equation we get the following relation for the proper time τ

$$\begin{aligned} \tau = & \frac{1}{2\sqrt{2}q\sqrt{r_0}\sqrt{\frac{q}{\sqrt{a^2-8Mq+a}}}\sqrt{a+\frac{2M}{r_0}+qr_0}} \left(\left(\sqrt{a^2-8Mq}-a\right)\sqrt{\frac{-r_0\sqrt{a^2-8Mq}+ar_0+4M}{M}} \right. \\ & \times \left(\sqrt{\frac{2qr_0}{a-\sqrt{a^2-8Mq}}} + 1\mathcal{E} \left(\sinh^{-1} \left(\sqrt{2}\sqrt{r_0}\sqrt{\frac{q}{\sqrt{a^2-8Mq+a}}} \right) \Big| \frac{a\left(\sqrt{a^2-8Mq}+a\right)-4Mq}{4Mq} \right) \right. \\ & \left. \left. - \mathcal{F} \left(\sinh^{-1} \left(\sqrt{2}\sqrt{r_0}\sqrt{\frac{q}{\sqrt{a^2-8Mq+a}}} \right) \Big| \frac{a\left(\sqrt{a^2-8Mq}+a\right)-4Mq}{4Mq} \right) \right) \right) \end{aligned}$$

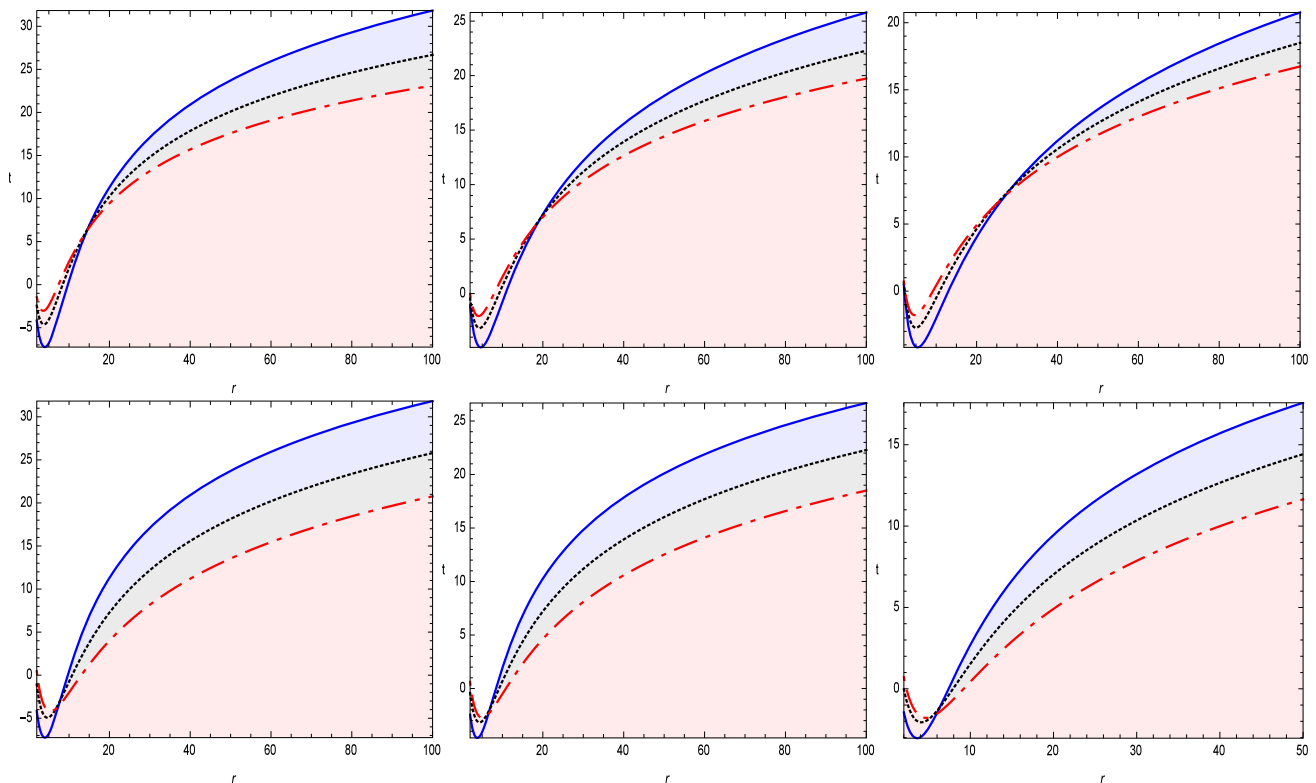


Fig. 3 Shows the behavior of t for the different possible values of a and q . The left panel of the first row represents $q = 0.05$ (blue), $q = 0.06$ (black), and $q = 0.07$ (red) with $a = 0.7$. The middle panel of the first row represents $q = 0.05$ (blue), $q = 0.06$ (black), and $q = 0.07$ (red) with $a = 0.8$. The right panel of the first row represents $q = 0.05$ (blue), $q = 0.06$ (black), and $q = 0.07$ (red) with $a = 0.9$. The left

panel of the second row represents $a = 0.7$ (blue), $a = 0.8$ (black), and $a = 0.9$ (red) with $q = 0.05$. The middle panel of the second row represents $a = 0.7$ (blue), $a = 0.8$ (black), and $a = 0.9$ (red) with $q = 0.06$. The right panel of the second row represents $a = 0.7$ (blue), $a = 0.8$ (black), and $a = 0.9$ (red) with $q = 0.07$

$$\begin{aligned}
 & - \left(\frac{1}{2\sqrt{2}q\sqrt{r}\sqrt{\frac{q}{\sqrt{a^2-8Mq+a}}}\sqrt{a+\frac{2M}{r}+qr}} \left(\left(\sqrt{a^2-8Mq}-a \right) \sqrt{\frac{-r\sqrt{a^2-8Mq}+ar+4M}{M}} \right. \right. \\
 & \times \left(\sqrt{\frac{2qr}{a-\sqrt{a^2-8Mq}}} + 1 \mathcal{E} \left(\sinh^{-1} \left(\sqrt{2}\sqrt{r}\sqrt{\frac{q}{\sqrt{a^2-8Mq+a}}} \right) \left| \frac{a(\sqrt{a^2-8Mq}+a)-4Mq}{4Mq} \right. \right) \right. \\
 & \left. \left. \left. - \mathcal{F} \left(\sinh^{-1} \left(\sqrt{2}\sqrt{r}\sqrt{\frac{q}{\sqrt{a^2-8Mq+a}}} \right) \left| \frac{a(\sqrt{a^2-8Mq}+a)-4Mq}{4Mq} \right. \right) \right) \right) \right), \tag{19}
 \end{aligned}$$

where \mathcal{F} and \mathcal{E} are the elliptic integrals of the first and second kind respectively. Here τ is the time of approach of the massive particles towards the central object, measured by the observer in the rest frame, in radial motion. From its graphic behavior in the Fig. 4 it can be seen that with increase in the value of the quintessence parameter q , the proper time τ decreases while with the increase in the values of the string cloud parameter a it increases.

The effective potential of the massive particles in radial motion is given as

$$V_{eff}(r) = \left(1 - a - \frac{2M}{r} - \frac{q}{r^{-1}} \right). \tag{20}$$

In the Figs. 5 and 6, the behavior of $V_{eff}(r)$ is revealed for a unit mass black hole. This shows that the effective potential for the timelike geodesics in the radial motion decreases with

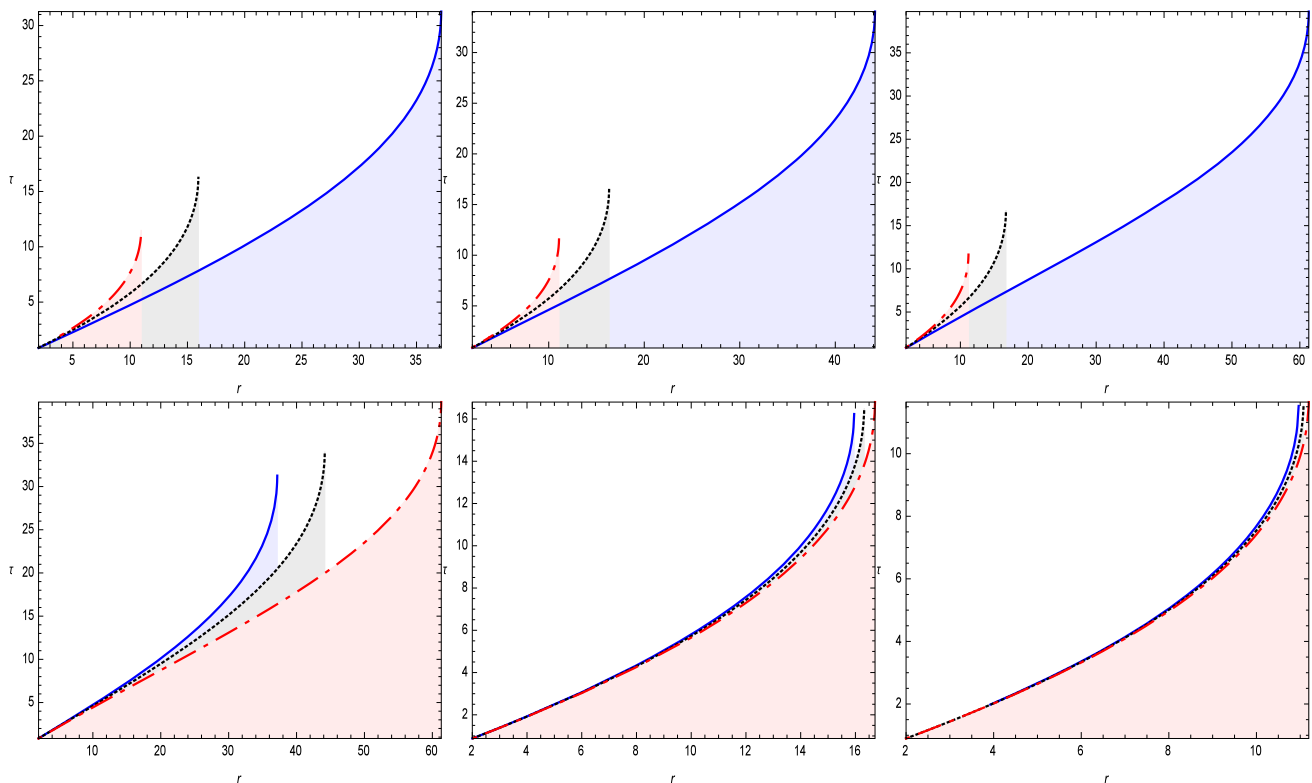


Fig. 4 Shows the behavior of τ for the different possible values of a and q . The left panel of the first row represents $a = 0.1$ (blue), $a = 0.15$ (black), and $a = 0.2$ (red) with $q = 0.0010$. The middle panel of the first row represents $a = 0.1$ (blue), $a = 0.15$ (black), and $a = 0.2$ (red) with $q = 0.0011$. The right panel of the first row represents $a = 0.1$ (blue), $a = 0.15$ (black), and $a = 0.2$ (red) with $q = 0.0012$. The left

panel of the second row represents $q = 0.0010$ (blue), $q = 0.0011$ (black), and $q = 0.0012$ (red) with $q = 0.1$. The middle panel of the second row represents $q = 0.0010$ (blue), $q = 0.0011$ (black), and $q = 0.0012$ (red) with $q = 0.15$. The right panel of the second row represents $q = 0.0010$ (blue), $q = 0.0011$ (black), and $q = 0.0012$ (red) with $q = 0.2$

the increasing values of the string cloud parameter a and the quintessence parameter q . In the same Figs. 5 and 6, the regions of positive and negative effective potentials are also shown for different values of a and q .

From Eq. (4) with Eq. (9), we get the following relation

$$\left(\frac{dr}{dt}\right)^2 = \frac{(-a - \frac{2M}{r} - qr + 1)^2 (E^2 - (-a - \frac{2M}{r} - qr + 1))}{E^2 r^3} \tag{21}$$

On solving the Eq. (21), we get the following expression

$$t = \frac{l_1 l_2}{q^2 r^2 \sqrt{\frac{(r(a+qr-1)+2M)^2 (r(a+qr+E^2-1)+2M)}{E^2 r^3}}} \times \left(\frac{l_9 \text{EllipticPi}(l_{10}; l_7 | l_8)}{l_{11} \sqrt{(a-1)^2 - 8Mq}} - \frac{l_5 \text{EllipticPi}(l_6; l_7 | l_8)}{l_{11}} + \text{EllipticF}(l_3 | l_4) \right) \tag{22}$$

where EllipticPi , EllipticF are special functions, and $l_j (j = 1 \dots 12)$ are given in Appendix I.

From the graphical behavior of t given in Fig. 7, it is clear that t decreases as the values of both the parameters q and

a increase. Thus in the presence of quintessence and string clouds a test particle takes longer to reach the horizon of the black hole as compared to the pure Schwarzschild case.

4 Circular motion

In this section we examine the circular motion of massive particles and photons. The expressions for energy E^2 and angular momentum L^2 are given below whose graphical behavior is shown in Figs. 8 and 9 for different values of the parameters a and q .

$$E^2 = \frac{2r}{r^2 \left(-\frac{2}{r(a+qr-1)+2M} - q \right) + 2M} \tag{23}$$

$$L^2 = \frac{r^4 \left(q - \frac{2M}{r^2} \right)}{r^2 \left(-\frac{2}{r(a+qr-1)+2M} - q \right) + 2M} \tag{24}$$

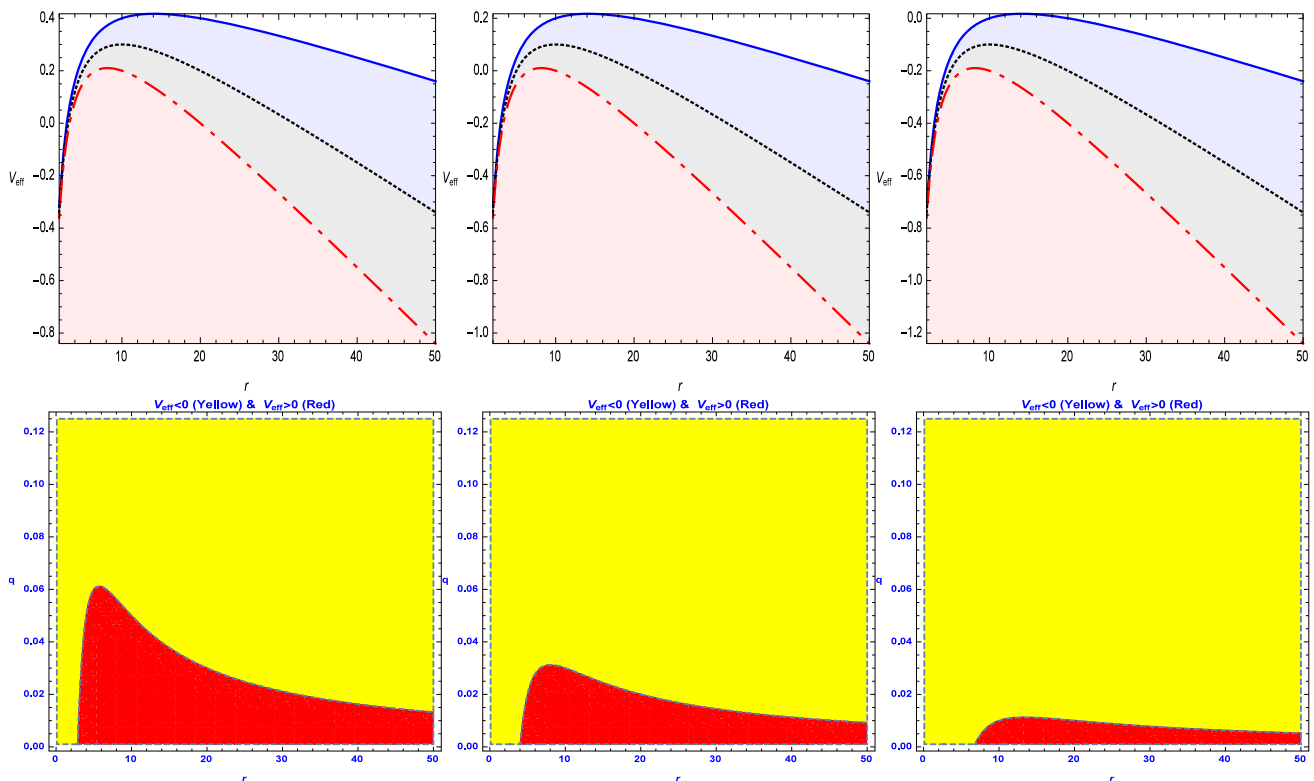


Fig. 5 Shows the behavior of $V_{eff}(r)$ for the different possible values of a and q . The left panel of the first row represents $q = 0.01$ (blue), $q = 0.02$ (black), and $q = 0.03$ (red) with $a = 0.3$. The middle panel of the first row represents $q = 0.01$ (blue), $q = 0.02$ (black), and $q = 0.03$ (red) with $a = 0.5$. The right panel of the first row represents

$q = 0.01$ (blue), $q = 0.02$ (black), and $q = 0.03$ (red) with $a = 0.7$. The second row shows the positive and negative region of $V_{eff}(r)$ for three different values of $a = 0.3$ (left panel), $a = 0.5$ (middle panel), and $a = 0.7$ (right panel)

5 Null case

The derivative of the effective potential, given by Eq. (8), when $\zeta = 0$ is expressed as

$$\frac{dV_{eff}(r)}{dr} = \frac{L^2 \left(\frac{2M}{r^2} - q \right)}{r^2} - \frac{2L^2 \left(-a - \frac{2M}{r} - qr + 1 \right)}{r^3}. \tag{25}$$

The radii of the unstable photon orbit can be derived by taking $\frac{dV_{eff}(r)}{dr} = 0$ as

$$\begin{aligned} r_q^N &= \frac{1 - a - \sqrt{a^2 - 2a - 6Mq + 1}}{q}, \\ r_e^N &= \frac{1 - a + \sqrt{a^2 - 2a - 6Mq + 1}}{q}. \end{aligned} \tag{26}$$

In the required limit r_e^N , reduces to that for the Schwarzschild case. The r_q^N , is due to the presence of the quintessence field.

The graphical behavior of r_e^N and r_q^N , can be seen from Figs. 10 and 11 respectively.

The graphical analysis of V_{eff}^N is given in the Fig. 12.

6 Timelike case

Here we calculate the derivative of the effective potential given by Eq. (8), for the timelike geodesics i.e., when $\zeta = 1$, as

$$\begin{aligned} \frac{dV_{eff}(r)}{dr} &= \left(\frac{L^2}{r^2} + 1 \right) \left(\frac{2M}{r^2} - q \right) \\ &\quad - \frac{2L^2 \left(-a - \frac{2M}{r} - qr + 1 \right)}{r^3}. \end{aligned} \tag{27}$$

To find the radii of the circular orbits for massive particles we put $\frac{dV_{eff}(r)}{dr} = 0$, which gives us

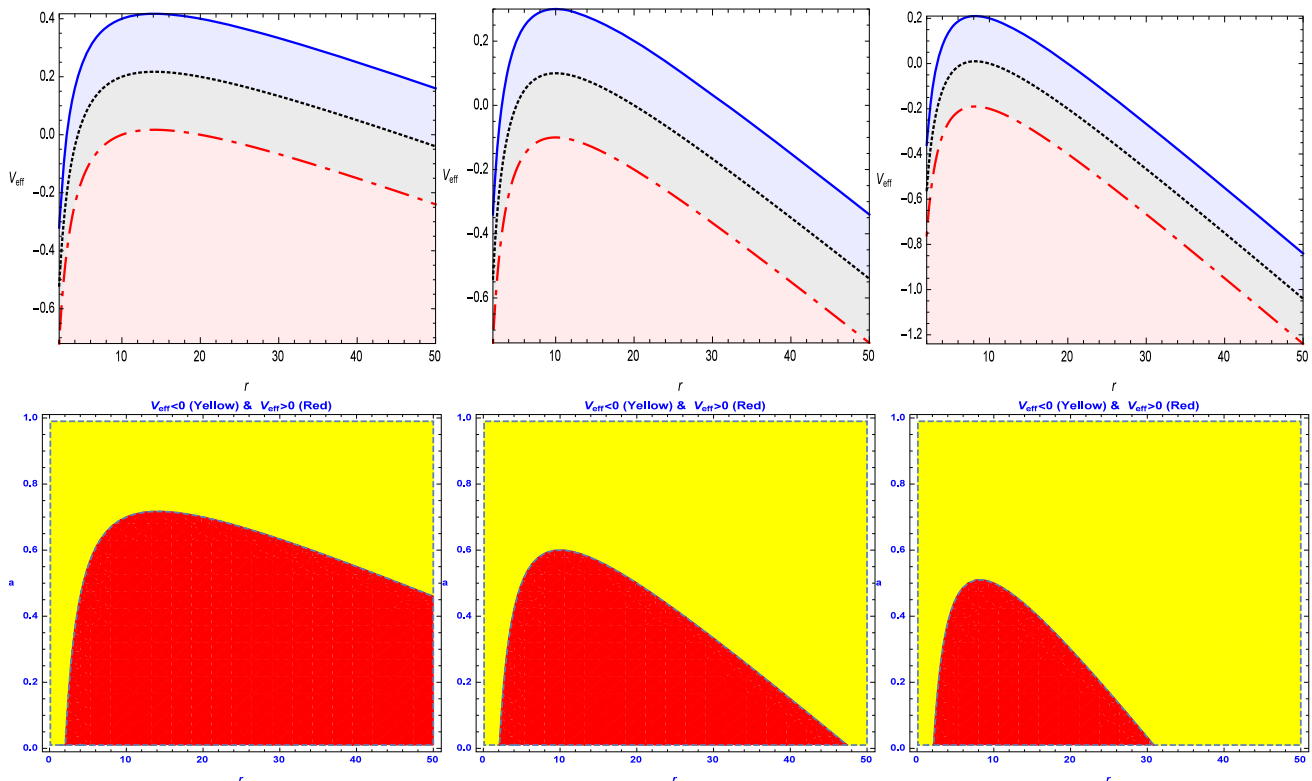


Fig. 6 Shows the behavior of $V_{eff}(r)$ for the different possible values of a and q . The left panel of the first row represents $a = 0.3$ (blue), $a = 0.5$ (black), and $a = 0.7$ (red) with $q = 0.01$. The middle panel of the first row represents $a = 0.3$ (blue), $a = 0.5$ (black), and $a = 0.7$ (red) with $q = 0.02$. The right panel of the first row represents $a = 0.3$ (blue), $a = 0.5$ (black), and $a = 0.7$ (red) with $q = 0.03$. The second row shows the positive and negative region of $V_{eff}(r)$ for three different values of q = 0.01 (left panel), $q = 0.02$ (middle panel), and $q = 0.03$ (right panel)

$$r_b^P = -\frac{1}{2} \sqrt{-\frac{L^2(-q) - 2M}{q} - \frac{L^2q + 2M}{3q} - \frac{\sqrt[3]{2}(L^4q^2 - 68L^2Mq + 4M^2)}{3q\sqrt[3]{\Psi_1 + \Psi_2}} - \frac{\sqrt[3]{\Psi_1 + \Psi_2}}{3\sqrt[3]{2q}}} + \frac{1}{2} \times \sqrt{-\frac{4(aL^2 - L^2)}{\Psi_3} + \frac{L^2q + 2M}{3q} - \frac{L^2(-q) - 2M}{q} + \frac{\sqrt[3]{2}(L^4q^2 - 68L^2Mq + 4M^2)}{3q\sqrt[3]{\Psi_1 + \Psi_2}} + \frac{\sqrt[3]{\Psi_1 + \Psi_2}}{3\sqrt[3]{2q}}} \tag{28}$$

where

$$\begin{aligned} \Psi_1 &= \sqrt{\left(-108q(aL^2 - L^2)^2 + 2(L^2q + 2M)^3 + 432L^2Mq(L^2q + 2M)\right)^2 - 4\left((L^2q + 2M)^2 - 72L^2Mq\right)^3}, \\ \Psi_2 &= -108q(aL^2 - L^2)^2 + 2(L^2q + 2M)^3 + 432L^2Mq(L^2q + 2M), \\ \Psi_3 &= q \sqrt{-\frac{L^2(-q) - 2M}{q} - \frac{L^2q + 2M}{3q} - \frac{\sqrt[3]{2}(L^4q^2 - 68L^2Mq + 4M^2)}{3q\sqrt[3]{\Psi_1 + \Psi_2}} - \frac{\sqrt[3]{\Psi_1 + \Psi_2}}{3\sqrt[3]{2q}}}. \end{aligned}$$

The behavior of the r_b^P can be checked from the Fig. 13. The V_{eff}^P is calculated as

$$V_{eff}^P = \left(\frac{L^2}{r^2} + 1\right) \left(-a - \frac{2M}{r} - \frac{q}{r} + 1\right). \tag{29}$$

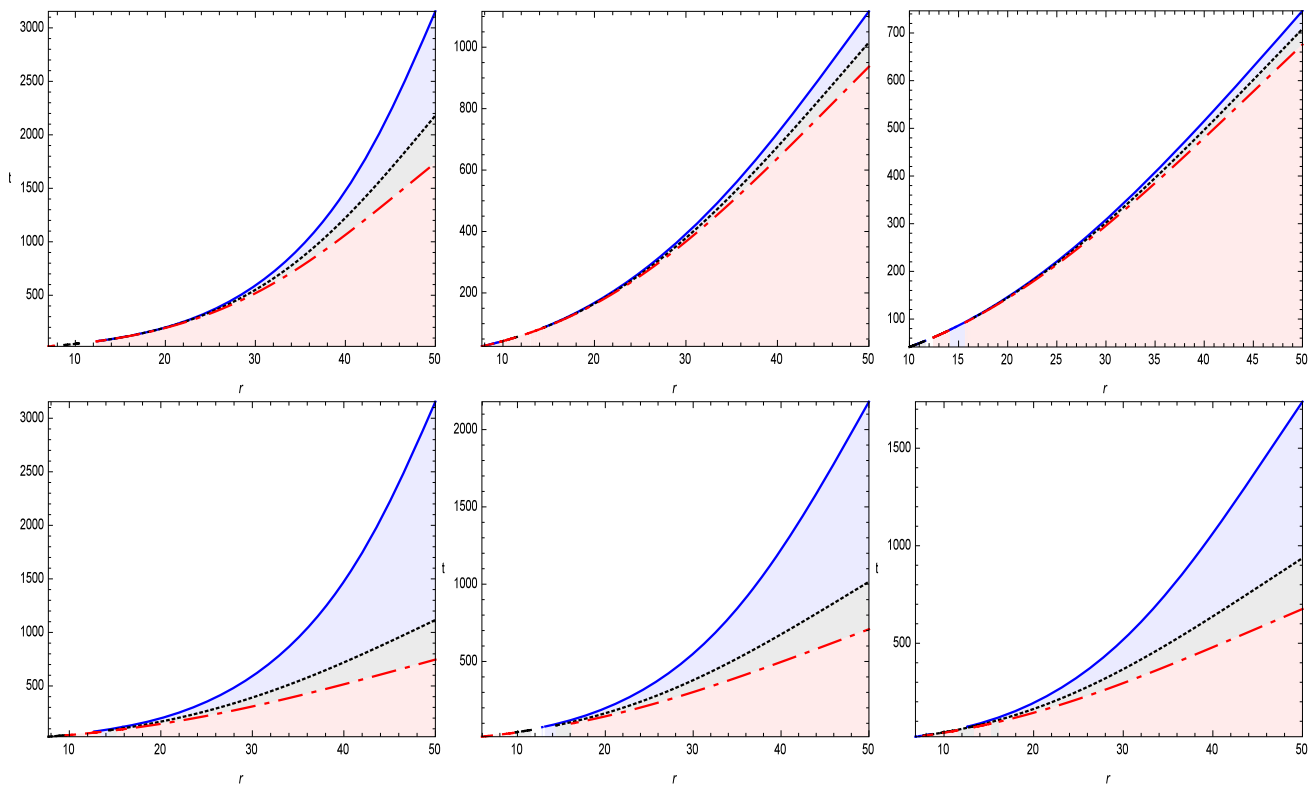


Fig. 7 Shows the behavior of t for the different possible values of a and q . The left panel of the first row represents $q = 0.007$ (blue), $q = 0.008$ (black), and $q = 0.009$ (red) with $a = 0.93$. The middle panel of the first row represents $q = 0.007$ (blue), $q = 0.008$ (black), and $q = 0.009$ (red) with $a = 0.95$. The right panel of the first row represents $q = 0.007$ (blue), $q = 0.008$ (black), and $q = 0.009$ (red)

with $a = 0.97$. The left panel of the second row represents $a = 0.93$ (blue), $a = 0.95$ (black), and $a = 0.97$ (red) with $q = 0.007$. The middle panel of the second row represents $a = 0.93$ (blue), $a = 0.95$ (black), and $a = 0.97$ (red) with $q = 0.008$. The right panel of the second row represents $a = 0.93$ (blue), $a = 0.95$ (black), and $a = 0.97$ (red) with $q = 0.009$

The behavior of V_{eff}^P can be seen from the Fig. 14. Here we see that the stable circular orbits exist for small positive values of both the parameters i.e. for $0 < a \ll 1$ and $0 < q \ll 1$.

7 Summary

In this article we have investigated the dynamics of massive particles and photons in the Schwarzschild black hole with string clouds and quintessence scalar field. We have found upper and lower bounds on the values of the string cloud parameter a and the quintessence parameter q , for the existence of black hole horizon, which are shown in Fig. 1. The Schwarzschild black hole surrounded by string clouds and quintessence field exists only for $0 < a < 1$ and $0 < q < 0.125$. For these values of a and q two horizons r_q and r_e of the black hole exist, given in Eq. (2). The r_q is purely due to the quintessence field while the r_e is the event horizon, which reduces to that of the Schwarzschild black hole when both the parameters a and q vanish. The behavior

of r_q and r_e is shown in Fig. 2 for different values of the parameters a and q .

We have discussed the radial geodesics of null and timelike particles for the allowed ranges of the parameters a and q . In the null particle case, we have found that if the values of the parameters a and q increase then the coordinate time t first decreases and then after crossing a turning point it increases with the increasing values of the parameter q , which is shown in Fig. 3. Thus in the presence of the string clouds and quintessence field for an external observer the particle will take shorter to reach the event horizon of the black hole as compared to the case of the pure Schwarzschild black hole, i.e. without string clouds and quintessence. In the case of the timelike radial geodesics the proper time τ decreases as a increases and it increases with increase in the values of the parameter q , shown in Fig. 4. In the same case the behavior of the coordinate time t is shown in Fig. 7 against the radial coordinate r for different values of the parameters a and q . With increase in the values of both the parameters a and q the time t decreases. This shows that in the presence of the string clouds and quintessence field the particle will reach earlier

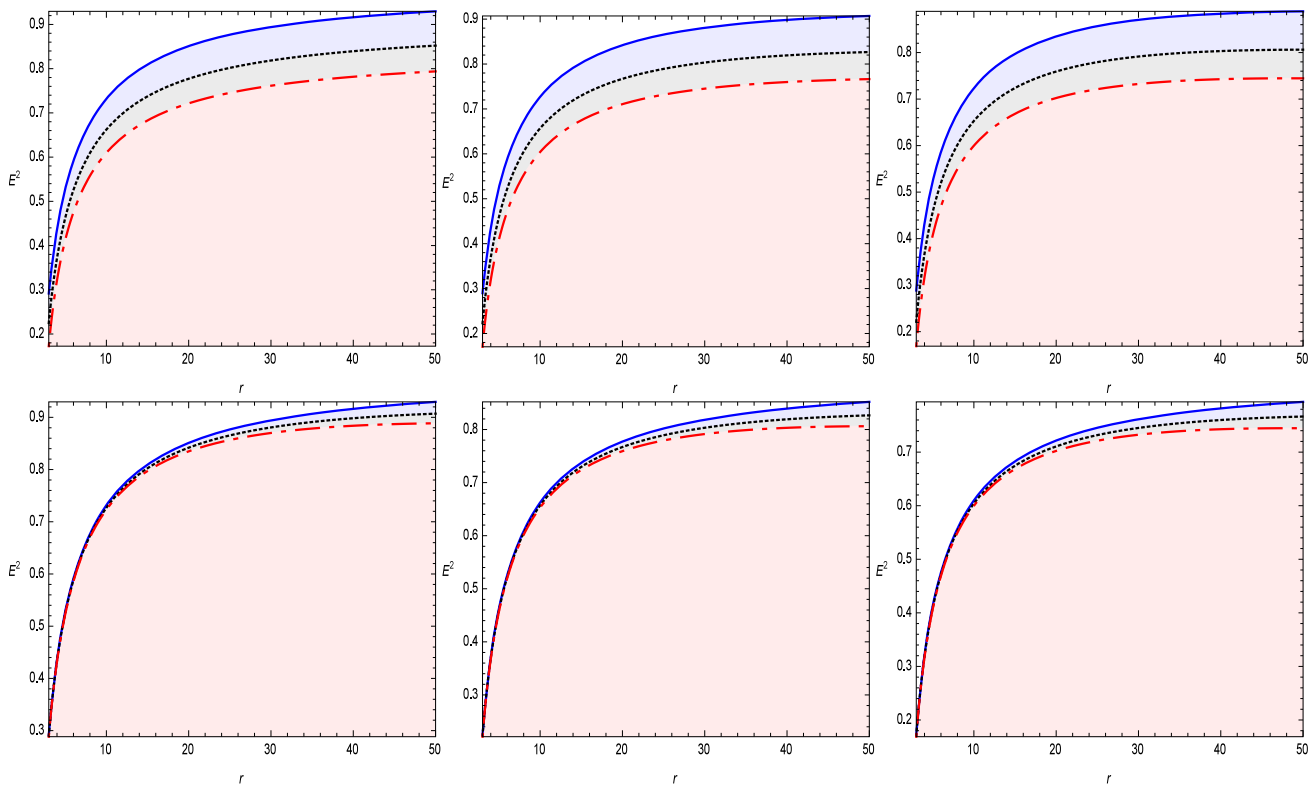


Fig. 8 Shows the behavior of E^2 for the different possible values of a and q . The left panel of the first row represents $q = 0.05$ (blue), $q = 0.06$ (black), and $q = 0.07$ (red) with $a = 0.7$. The middle panel of the first row represents $q = 0.05$ (blue), $q = 0.06$ (black), and $q = 0.07$ (red) with $a = 0.8$. The right panel of the first row represents $q = 0.05$ (blue), $q = 0.06$ (black), and $q = 0.07$ (red) with $a = 0.9$.

The left panel of the second row represents $a = 0.7$ (blue), $a = 0.8$ (black), and $a = 0.9$ (red) with $q = 0.05$. The middle panel of the second row represents $a = 0.7$ (blue), $a = 0.8$ (black), and $a = 0.9$ (red) with $q = 0.06$. The right panel of the second row represents $a = 0.7$ (blue), $a = 0.8$ (black), and $a = 0.9$ (red) with $q = 0.07$.

to the event horizon of the black hole as compared with the case of the pure Schwarzschild black hole. It is evident from Eq. (14) that the test particle will accelerate more rapidly towards the black hole in the presence of the quintessence scalar field. In the Figs. 5 and 6, the behavior of the effective potential is given which shows that the effective potential for the massive particles in the radial motion decreases with increase in the values of the string cloud parameter a and the quintessence parameter q .

Further we have discussed the circular motion of both the massive and massless particles for the permitted values of the parameters a and q . For the allowed values of the angular momentum L and energy E , it is obtained that the stable circular orbits of the test particles exist for very small values

of the string cloud parameter and the quintessence field i.e. for $0 < a \ll 1$ and $0 < q \ll 1$, shown in Fig. 14. We have observed that the radii of the unstable photon circular orbits increase as the values of the parameters a and q increase, shown in Fig. 10. In the case of the stable circular orbits of the test particles the radii of the orbits increase as the values of a increase and with an increase in q they go on decreasing, as shown in Fig. 13. Here we see that for massive particles the behavior of string clouds is repulsive. While the quintessence field when combined with string clouds behave attractive for massive particles. It should be noted that in the absence of quintessence field, our obtained results coincide with those of the Schwarzschild black hole with string clouds [13].

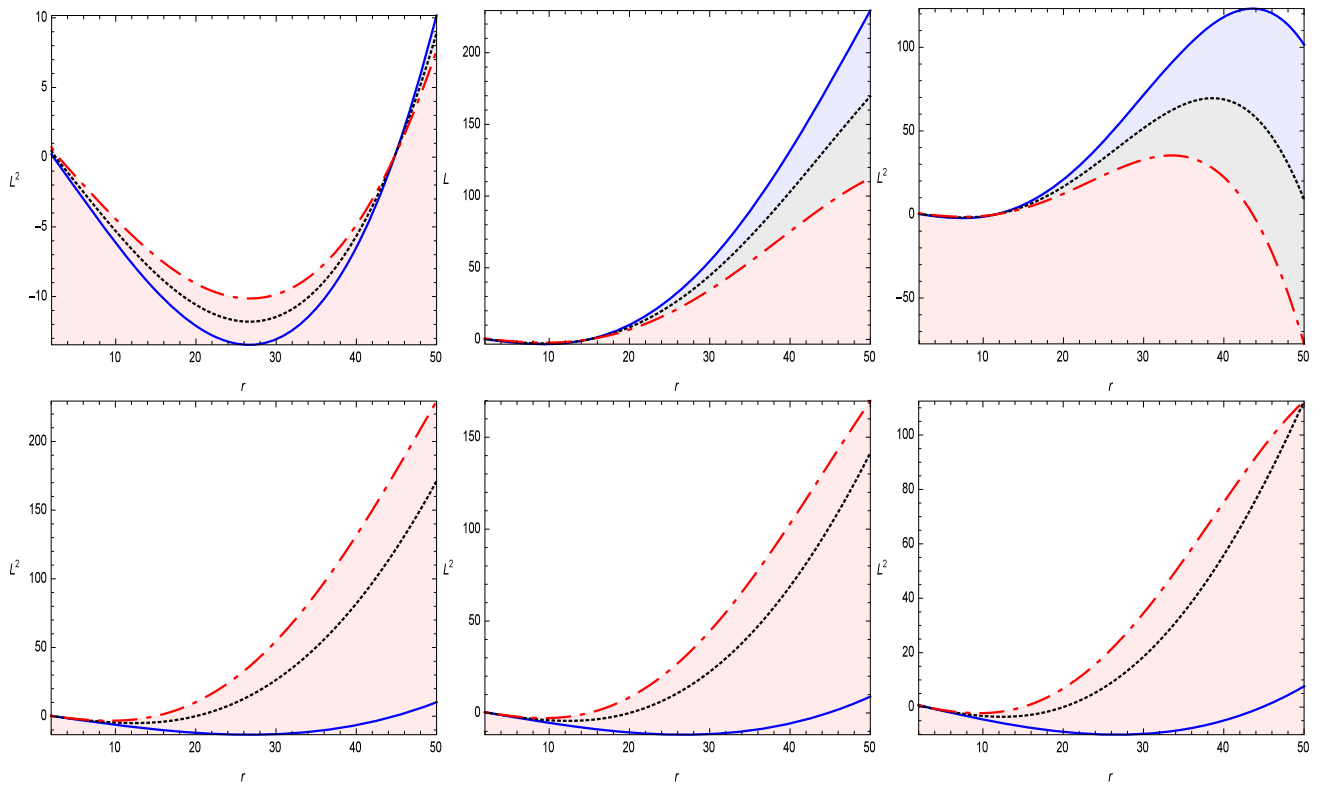


Fig. 9 Shows the behavior of L^2 for the different possible values of a and q . The left panel of the first row represents $q = 0.01$ (blue), $q = 0.02$ (black), and $q = 0.03$ (red) with $a = 0.1$. The middle panel of the first row represents $q = 0.01$ (blue), $q = 0.02$ (black), and $q = 0.03$ (red) with $a = 0.2$. The right panel of the first row represents $q = 0.01$ (blue), $q = 0.02$ (black), and $q = 0.03$ (red) with $a = 0.3$.

The left panel of the second row represents $a = 0.1$ (blue), $a = 0.2$ (black), and $a = 0.3$ (red) with $q = 0.01$. The middle panel of the second row represents $a = 0.1$ (blue), $a = 0.2$ (black), and $a = 0.3$ (red) with $q = 0.02$. The right panel of the second row represents $a = 0.1$ (blue), $a = 0.2$ (black), and $a = 0.3$ (red) with $q = 0.03$.

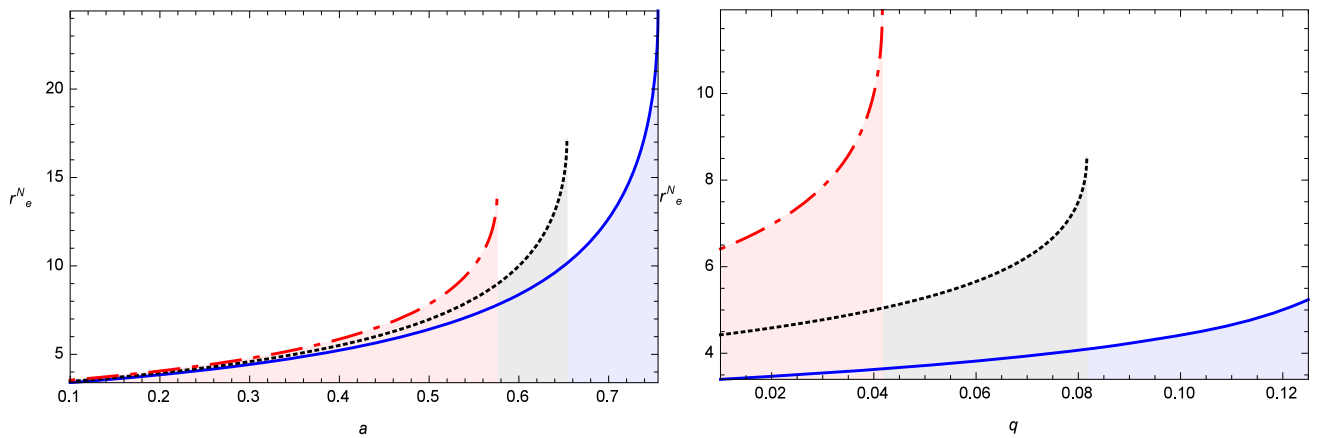


Fig. 10 Shows the graphic analysis of r_b^N (negative). The left panel represents $q = 0.01$ (blue), $q = 0.02$ (black), and $q = 0.03$ (red). The right panel represents $a = 0.1$ (blue), $a = 0.3$ (black), and $a = 0.5$ (red)

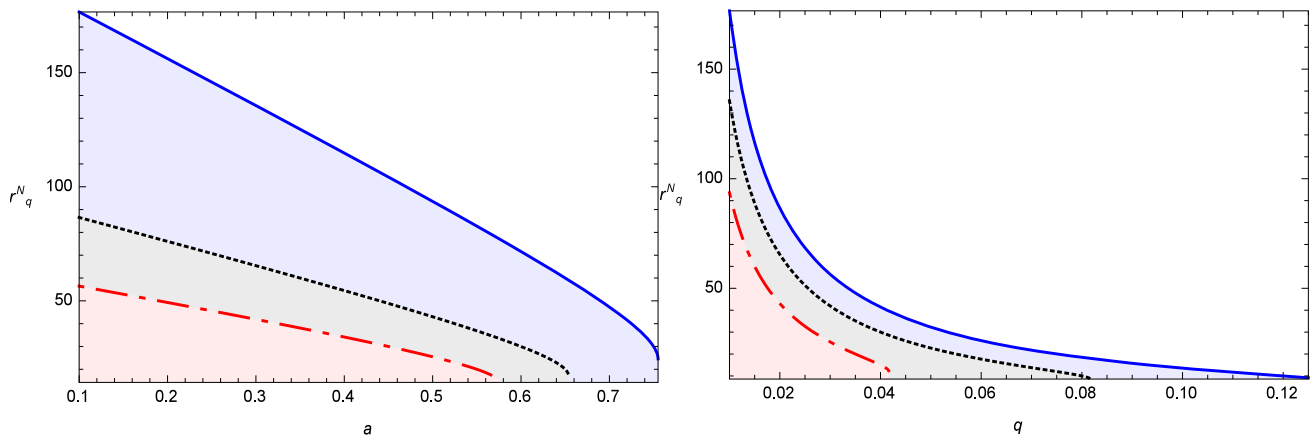


Fig. 11 Shows the graphic analysis of r_b^N . The left panel represents $q = 0.01$ (blue), $q = 0.02$ (black), and $q = 0.03$ (red). The right panel represents $a = 0.1$ (blue), $a = 0.3$ (black), and $a = 0.5$ (red)

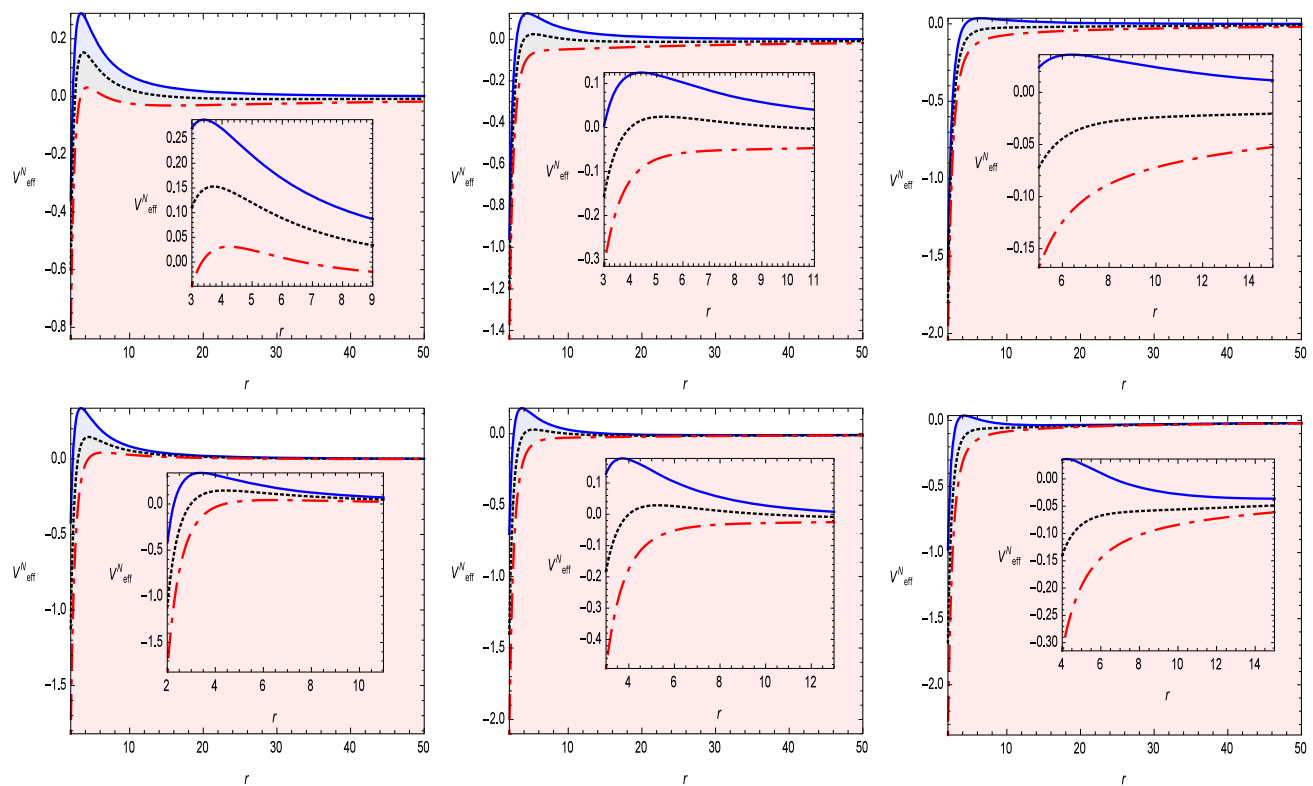


Fig. 12 Shows the behavior of V_{eff}^N for the different possible values of a and q . The left panel of the first row represents $a = 0.1$ (blue), $a = 0.3$ (black), and $a = 0.5$ (red) with $q = 0.01$. The middle panel of the first row represents $a = 0.1$ (blue), $a = 0.3$ (black), and $a = 0.5$ (red) with $q = 0.05$. The right panel of the first row represents $q = 0.01$ (blue), $q = 0.05$ (black), and $a = 0.09$ (red) with $a = 0.1$. The middle panel of first row represents $q = 0.01$ (blue), $q = 0.05$ (black), and $a = 0.09$ (red) with $a = 0.3$. The right panel of the first row represents $q = 0.01$ (blue), $q = 0.05$ (black), and $a = 0.09$ (red) with $a = 0.5$. The second row shows $q = 0.01$ (blue), $q = 0.05$ (black), and $a = 0.09$ (red) with $a = 0.1$. The middle panel of first row represents $q = 0.01$ (blue), $q = 0.05$ (black), and $a = 0.09$ (red) with $a = 0.3$. The right panel of the first row represents $q = 0.01$ (blue), $q = 0.05$ (black), and $a = 0.09$ (red) with $a = 0.5$

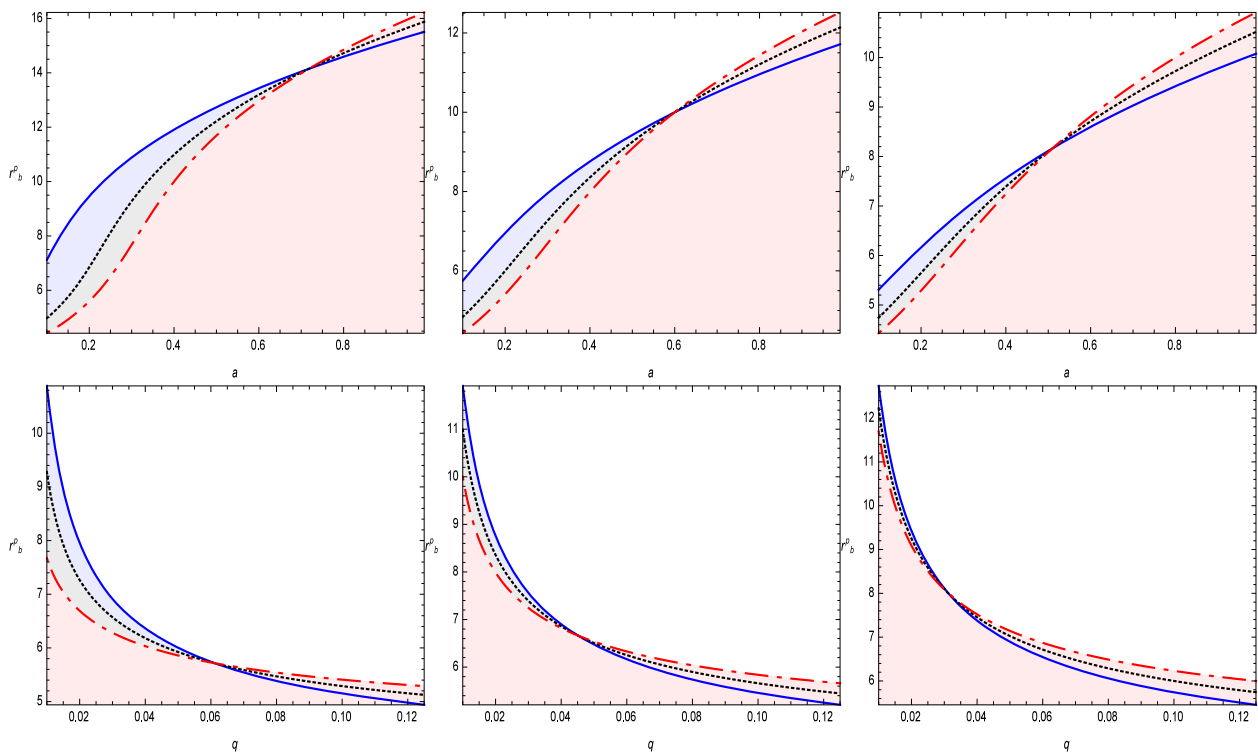


Fig. 13 Shows the behavior of r_b^p for the different possible values of a , L , and q . The left panel of the first row represents $L = \sqrt{12}$ (blue), $L = \sqrt{16}$ (black), and $L = \sqrt{20}$ (red) with $q = 0.01$. The middle panel of the first row represents $L = \sqrt{12}$ (blue), $L = \sqrt{16}$ (black), and $L = \sqrt{20}$ (red) with $q = 0.02$. The right panel of the first row represents $L = \sqrt{12}$ (blue), $L = \sqrt{16}$ (black), and $L = \sqrt{20}$ (red)

with $q = 0.03$. The left panel of the second row represents $L = \sqrt{12}$ (blue), $L = \sqrt{16}$ (black), and $L = \sqrt{20}$ (red) with $a = 0.1$. The middle panel of the second row represents $L = \sqrt{12}$ (blue), $L = \sqrt{16}$ (black), and $L = \sqrt{20}$ (red) with $a = 0.3$. The right panel of the second row represents $L = \sqrt{12}$ (blue), $L = \sqrt{16}$ (black), and $L = \sqrt{20}$ (red) with $a = 0.5$

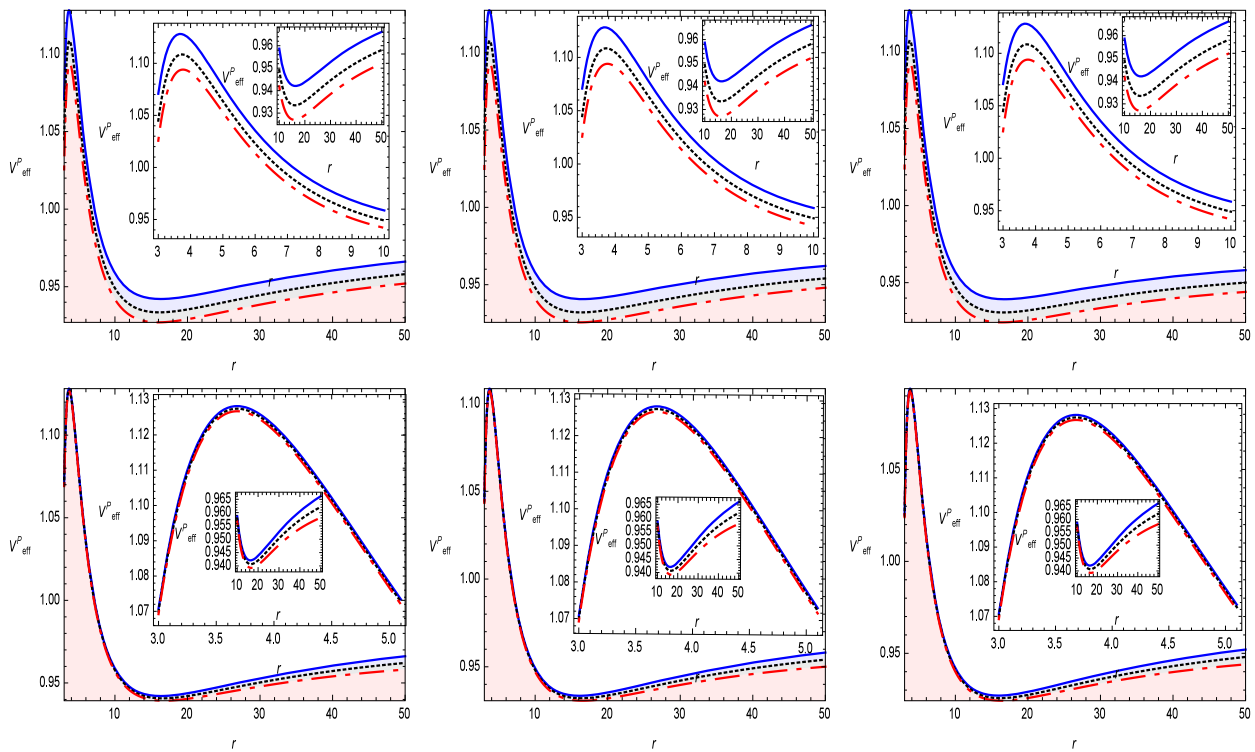


Fig. 14 Shows the behavior of V_{eff}^p for the different possible values of a and q . The left panel of the first row represents $a = 0.001$ (blue), $a = 0.009$ (black), and $a = 0.015$ (red) with $q = 0.00001$. The middle panel of the first row represents $a = 0.001$ (blue), $a = 0.009$ (black), and $a = 0.015$ (red) with $q = 0.00009$. The right panel of the first row represents $a = 0.001$ (blue), $a = 0.009$ (black), and

$a = 0.015$ (red) with $q = 0.00015$. The left panel of the second row represents $q = 0.00001$ (blue), $q = 0.00009$ (black), and $q = 0.00017$ (red) with $a = 0.001$. The middle panel of the second row represents $q = 0.00001$ (blue), $q = 0.00009$ (black), and $q = 0.00017$ (red) with $a = 0.009$. The right panel of the second row represents $q = 0.00001$ (blue), $q = 0.00009$ (black), and $q = 0.00017$ (red) with $a = 0.015$

Data Availability Statement This manuscript has no associated data or the data will not be deposited. [Authors' comment: There is no observational data.]

Open Access This article is licensed under a Creative Commons Attribution 4.0 International License, which permits use, sharing, adaptation, distribution and reproduction in any medium or format, as long as you give appropriate credit to the original author(s) and the source, provide a link to the Creative Commons licence, and indicate if changes were made. The images or other third party material in this article are included in the article's Creative Commons licence, unless indicated otherwise in a credit line to the material. If material is not included in the article's Creative Commons licence and your intended use is not permitted by statutory regulation or exceeds the permitted use, you will need to obtain permission directly from the copyright holder. To view a copy of this licence, visit <http://creativecommons.org/licenses/by/4.0/>.
Funded by SCOAP³.

Appendix I

$$l_1 = 2\sqrt{2}\sqrt{(a + E^2 - 1)^2 - 8Mq}$$

$$\times \sqrt{\frac{qr}{\sqrt{(a + E^2 - 1)^2 - 8Mq} + a + E^2 - 1}}$$

$$l_2 = (r(a + qr - 1) + 2M)$$

$$\times \sqrt{\frac{q(r(a + qr + E^2 - 1) + 2M)}{(a + E^2 - 1)^2 - 8Mq}}$$

$$l_3 = \sin^{-1} \left(\frac{\sqrt{\frac{\sqrt{(a + E^2 - 1)^2 - 8Mq} + a + 2qr + E^2 - 1}}{\sqrt{(a + E^2 - 1)^2 - 8Mq}}}{\sqrt{2}} \right),$$

$$l_4 = \frac{2\sqrt{(a + E^2 - 1)^2 - 8Mq}}{\sqrt{(a + E^2 - 1)^2 - 8Mq} + a + E^2 - 1}$$

$$l_5 = \sqrt{(a - 1)^2 - 8Mq}$$

$$- a \left(\sqrt{(a - 1)^2 - 8Mq} + a - 2 \right) + 4Mq - 1,$$

$$l_6 = \frac{2\sqrt{(a + E^2 - 1)^2 - 8Mq}}{-\sqrt{(a - 1)^2 - 8Mq} + \sqrt{(a + E^2 - 1)^2 - 8Mq} + E^2}$$

$$l_7 = \sin^{-1} \left(\frac{\sqrt{\frac{\sqrt{(a+E^2-1)^2-8Mq+a+2qr+E^2-1}}{\sqrt{(a+E^2-1)^2-8Mq}}}}{\sqrt{2}} \right),$$

$$l_8 = \frac{2\sqrt{(a+E^2-1)^2-8Mq}}{\sqrt{(a+E^2-1)^2-8Mq+a+E^2-1}},$$

$$l_9 = -\sqrt{(a-1)^2-8Mq} + a \left(\sqrt{(a-1)^2-8Mq} - a + 2 \right) + 4Mq - 1,$$

$$l_{10} = \frac{2\sqrt{(a+E^2-1)^2-8Mq}}{\sqrt{(a-1)^2-8Mq} + \sqrt{(a+E^2-1)^2-8Mq+E^2}},$$

$$l_{11} = -\sqrt{(a-1)^2-8Mq} + \sqrt{(a+E^2-1)^2-8Mq+E^2},$$

$$l_{12} = \sqrt{(a-1)^2-8Mq} + \sqrt{(a+E^2-1)^2-8Mq+E^2}.$$

References

1. B.P. Abbott et al., Phys. Rev. Lett. **116**, 061102 (2016)
2. C.W. Misner, K.S. Thorne, J.A. Wheeler, *Gravitation* (W.H. Freeman and Company, San Francisco, 1973)
3. A.D. Ingram, S.E. Motta, New Astron. Rev. **85**, 101524 (2019)
4. D. Pugliese, H. Quevedo, R. Ruffini, Phys. Rev. D **83**, 024021 (2011)
5. D. Pugliese, H. Quevedo, R. Ruffini, Phys. Rev. D **83**, 104052 (2011)
6. D. Pugliese, H. Quevedo, R. Ruffini, Phys. Rev. D **84**, 044030 (2011)
7. D. Pugliese, H. Quevedo, R. Ruffini, Phys. Rev. D **88**, 024042 (2011)
8. V. Frolov, D. Stojkovic, Phys. Rev. D **68**, 064011 (2013)
9. A. Abdujabbarov, B. Ahmedov, Phys. Rev. D **81**, 044022 (2010)
10. S. Hussain, I. Hussain, M. Jamil, Eur. Phys. J. C **74**, 3210 (2014)
11. I. Hussain, B. Majeed, M. Jamil, Int. J. Theor. Phys. **54**, 1567 (2015)
12. I. Hussain, S. Ali, Eur. Phys. J. Plus **131**, 275 (2016)
13. M. Batool, I. Hussain, Int. Mod. Phys. D **26**, 1741005 (2017)
14. B. Jiri, S. Zdenek, B. Vladimir, Bull. Astron. Inst. Czechoslov. **40**, 65 (1989)
15. Y. Nakamura, T. Ishizuka, Astrophys. Space Sci. **210**, 105 (1993)
16. A.N. Aliev, N. Özdemir, Mon. Not. R. Astron. Soc. **336**, 241 (2002)
17. M. Olivares, J. Saavedra, C. Leiva, J.R. Villanueva, Mod. Phys. Lett. A **26**, 2923 (2011)
18. A. García, E. Hackmann, J. Kunz, C. Lämmerzahl, A. Macías, J. Math. Phys. **56**, 032501 (2015)
19. Z. Li, G. Zhang, A. Övgün, Phys. Rev. D **101**, 124058 (2020)
20. R.M. Wald, Phys. Rev. D **10**, 1680 (1974)
21. T. Damour, R.S. Hanni, R. Ruffini, J.R. Wilson, Phys. Rev. D **17**, 1518 (1978)
22. I.H. Salazar, A. Garcia, J. Plebanski, J. Math. Phys. **28**, 1271 (1987)
23. A. Abdujabbarov, B. Ahmedov, O. Rahimov, U. Salikhbaev, Phys. Scr. **89**, 084008 (2014)
24. B. Narzilloev, J. Rayimbaev, A. Abdujabbarov, C. Bambi, Eur. Phys. J. C **80**, 1074 (2020)
25. W. Javed, J. Abbas, A. Övgün, Ann. Phys. **418**, 168183 (2020)
26. A. Ditta, G. Abbas, Gen. Relativ. Gravit. **52**, 77 (2020)
27. G. Abbas, A. Mahmood, M. Zubairb, Phys. Dark Univ. **31**, 100750 (2021)
28. A. Abdujabbarov, F. Atamurotov, N. Dadhich, B. Ahmedov, Z. Stuchlík, Eur. Phys. J. C **75**, 399 (2015)
29. M. Sharif, M. Shahzadi, Eur. Phys. J. C **77**, 363 (2017)
30. C. Liu, T. Zhu, Q. Wu, K. Jusufi, M. Jamil, M. Azreg-Aïnou, A. Wang, Phys. Rev. D **101**, 084001 (2020)
31. J. Rayimbaev, A. Abdujabbarov, M. Jamil, B. Ahmedov, Wen-Biao Han, Phys. Rev. D **102**, 084016 (2020)
32. De-Cheng Zou, C. Wu, M. Zhang, R. Yue, Chin. Phys. C **44**, 055102 (2020)
33. Shao-Wen Wei, Yu-Xiao Liu, Chin. Phys. C **44**, 115103 (2020)
34. K. Jusufi, M. Azreg-Aïnou, M. Jamil, Shao-Wen Wei, Q. Wu, A. Wang, Phys. Rev. D **103**, 024013 (2021)
35. J. Liang, B. Mu, J. Tao, Chin. Phys. C **45**, 023121 (2021)
36. N. Dadhich, P.P. Kale, Pramana J. Phys. **9**, 71 (1977)
37. T. Müller, Am. J. Phys. **79**, 63 (2011)
38. W. Israel, Nature **209**, 66 (1996)
39. N. Cruz, M. Olivares, J.R. Villanueva, Class. Quantum Gravity **22**, 1167 (2005)
40. S. Fernando, Gen. Relativ. Gravit. **44**, 1857 (2012)
41. J.M. Toledo, V.B. Bezerra, Eur. Phys. J. C **78**, 534 (2018)
42. J.M. Toledo, V.B. Bezerra, Int. J. Mod. Phys. D **28**, 1950023 (2019)
43. V.V. Kiselev, Class. Quantum Gravity **20**, 1187 (2003)